

Efficient, stabilized two-qubit gates on a trapped-ion quantum computer

Reinhold Blümel,^{1,2} Nikodem Grzesiak,² Nhung H. Nguyen,³ Alaina M. Green,³
Ming Li,² Andrii Maksymov,² Norbert M. Linke,³ and Yunseong Nam²

¹Wesleyan University, Middletown, CT 06459, USA

²IonQ, College Park, MD 20740, USA

³Joint Quantum Institute, University of Maryland, College Park, MD 20742, USA

(Dated: January 21, 2021)

Quantum computing is currently limited by the cost of two-qubit entangling operations. In order to scale up quantum processors and achieve a quantum advantage, it is crucial to economize on the power requirement of two-qubit gates, make them robust to drift in experimental parameters, and shorten the gate times. In this paper, we present two methods, one exact and one approximate, to construct optimal pulses for entangling gates on a pair of ions within a trapped ion chain, one of the leading quantum computing architectures. Our methods are direct, non-iterative, and linear, and can construct gate-steering pulses requiring less power than the standard method by more than an order of magnitude in some parameter regimes. The power savings may generally be traded for reduced gate time and greater qubit connectivity. Additionally, our methods provide increased robustness to mode drift. We illustrate these trade-offs on a trapped-ion quantum computer.

Introduction.—For the growing number of programmable quantum computers available today [1–10], computational instructions for quantum applications are typically compiled into single- and two-qubit quantum gates [11–13]. At the physical, hardware-execution level, and in all current quantum-computer architectures, two-qubit gates are about one to two orders of magnitude more costly to implement than single-qubit gates [14, 15]. Therefore, improving two-qubit gate performance is critical to the utility and scalability of quantum computers.

For trapped ions, the best two-qubit gates are mediated by the harmonic motion through spin-dependent forces [16–19]. For laser-based gates in multi-ion chains, a range of pulse-shaping protocols has been devised to decouple the multiple motional modes from the qubit degree of freedom, such as amplitude modulation [7, 20–22], phase modulation [23], frequency modulation [24], or combinations thereof [25, 26]. These pulses can also create additional resilience to mode drift [25, 26] and gate-timing errors [26], enable fast gate action [27], or allow for simultaneous [28, 29] or multi-qubit [30] gates.

In [25] we reported a constructive method to calculate power-optimal pulse shapes based on the Mølmer-Sørensen protocol [17–19]. In practice, however, we expect a quantum gate to be imperfect due to limitations independent of the pulse shape, such as intensity fluctuations due to beam-power or beam-steering noise, motional-mode heating, motional dephasing, laser dephasing, off-resonant photon scattering, qubit dephasing or depolarization, and others. Therefore, we need not require mathematical exactness in constructing the pulse shape, but rather ensure that the error incurred by the imperfect pulse shape is much smaller than the other error mechanisms limiting the fidelity. Based on this strategy we present here a pulse-shaping technique that includes a systematic method of trading negligible amounts of fidelity for power savings of up to an order of magnitude under realistic operating conditions for a trapped-ion quantum computer. Alternatively, by trad-

ing power savings for gate speed, we are able to speed up two-qubit gates for a given power budget. We confirm this trade-off experimentally. This method also formulates gates which are naturally robust to mode-frequency drifts.

Protocol.—Implementation of the trade-off strategy is based on a provably power-optimal pulse-shaping method for laser-based radial-mode gates [25]. Using simultaneous amplitude- and frequency-modulation, it produces a gate with a theoretical fidelity of 1 for any given gate time τ and includes a systematic method for actively stabilizing the fidelity with respect to motional-mode frequency drift. We refer to this method as the exact AMFM method. The laser-control pulses $g(t)$ are represented as Fourier integrals, $g(t) = \int_{-\infty}^{\infty} A(\omega) \exp(i\omega t) dt$, which are subsequently discretized into a Fourier-sine series $g(t) = \sum_{n=1}^{N_A} A_n \sin(2\pi n t / \tau)$, where $N_A \sim 300$ achieves convergence for typical two-qubit gates with $\tau \sim 100 \mu\text{s}$. Thus, in contrast to previous methods that employ either a single [5, 7] or a few [26] laser-frequency tones, our method uses a quasi-continuum of frequencies resulting in a chirped pulse of the form $g(t) = \Omega(t) \sin[\psi(t)]$, where $\psi(t) = \int_0^t \mu(t') dt'$ and $\mu(t)$ is the detuning function. The resulting signal can be implemented straightforwardly with an arbitrary waveform generator. Phase-space closure requires $\alpha_p^i = -\eta_p^i \int_0^\tau g(t) \exp(i\omega_p t) = 0$, for $i, p = 1, \dots, N$, where p is the mode index, i the ion index, η_p^i the Lamb-Dicke parameter, ω_p the mode frequency, and N the ion number. Therefore, including stabilization against mode-frequency drift to an arbitrary order K , we require $\partial^K \alpha_p^i / \partial \omega_p^K = 0$. This represents $Q = N(K + 1)$ homogeneous, linear equations that, in matrix notation, may be written as $M \vec{A}^\gamma = 0$, where $\gamma = 1, \dots, N_A - Q$ and the set of nontrivial amplitude solutions, \vec{A}^γ , spans the null-space of the constraint matrix M . In general, the dimension N_A of the frequency space is much larger than Q , which leaves a large null-space to optimize the gate power. Introducing the aver-

age power, $\bar{P} = (1/\tau) \int_0^\tau g^2(t) dt = (1/2) \sum_{n=1}^{N_A} A_n^2$, the gate angle $\chi_{ij} = \vec{A}^T V^{ij} \vec{A}$ is achieved with the minimum \bar{P} , if \vec{A} is chosen as the eigenvector of V^{ij} associated with the eigenvalue of largest absolute value. V^{ij} is the null-space projected kernel matrix $\mathcal{K}_{nm}^{ij} = \sum_p \eta_p^i \eta_p^j \int_0^\tau dt_2 \int_0^{t_2} dt_1 \sin(2\pi n t_2 / \tau) \sin(2\pi m t_1 / \tau) \sin[\omega_p(t_2 - t_1)]$, which can be evaluated analytically since it contains only elementary functions. Since the ion number N does not occur explicitly other than in the vector space size, the method is naturally scalable to any number of ions. Since the method involves only linear algebra, it is computationally efficient and straightforward to implement. Additional linear conditions, for instance stabilization against gate-timing errors [26], may be added at will. Thus the method also scales in the number and types of stabilization conditions. However, if more conditions are added, the size of the null-space contracts, and with it the number of accessible degrees of freedom, which leads to an increase in the power required. Conversely, for a set of constraints and a given power budget, \bar{P} , there is a minimum gate-duration, τ_{\min} , which roughly follows $\tau_{\min} \sim 1/\bar{P}$ for gate times $\tau > 100 \mu\text{s}$. Thus, there is a trade-off between power requirement and gate duration.

Figure 1(a) shows the power requirement of the optimal, exact AMFM method for various qubit pairs (i, j) and degrees of stabilization K as a function of gate duration τ for a 15-ion chain, with an inter-ion spacing of $5 \mu\text{m}$ and the 11 central ions used as qubits. We see that the power requirement dramatically increases as we decrease τ , exhibiting a step-like transition, whose location is nearly independent of the specific ion-pair. The reason is the following. To operate a two-qubit gate at low power, it is necessary that the basis frequencies, $2\pi n t / \tau$, have good overlap with the motional-mode frequencies, $\omega_p \lesssim 2\pi \times 3 \text{ MHz}$. As τ decreases, more basis frequencies are pushed out of the frequency range of the motional modes, effectively reducing the dimension of the null-space from which the power-optimal solutions are drawn. The step in power results when we run out of null-space vectors with good motional-mode frequency overlap. Since increasing K reduces the null-space dimension even further, the power step happens at larger gate times τ for larger K . Similar to [27], our scheme cancels carrier excitations to first order due to the sinusoidal nature of our basis functions. While Fig. 1 shows gates $< 100 \mu\text{s}$, which remain approximately in the Lamb-Dicke regime, further investigation is needed to ensure the standard MS formalism with its perturbative expansions of the Hamiltonian is still valid in this short-pulse regime.

The two-qubit gate infidelity f at zero temperature is given by $f = 0.8 \vec{A}^T F \vec{A}$, where $F_{nm} = \sum_{p=1}^N [(\eta_p^i)^2 + (\eta_p^j)^2] \sigma_{np} \sigma_{mp}$ is the infidelity matrix and $\sigma_{np} = \int_0^\tau \sin(2\pi n t / \tau) \exp(i\omega_p t) dt$ [31]. The infidelity f may be systematically controlled by expanding the gate-pulse amplitudes \vec{A} in the set of eigenvectors \vec{W}_l of F that correspond to its smallest absolute eigenvalues up to $l = L_{\text{cut}}$, i.e. $\vec{A} = \sum_{l=1}^{L_{\text{cut}}} B_l \vec{W}_l$. The gate an-

gle is then given by $\chi_{ij} = \vec{A}^T \mathcal{K}^{ij} \vec{A} = \vec{B}^T S^{ij} \vec{B}$, where $S_{ll'}^{ij} = \vec{W}_l^T \mathcal{K}^{ij} \vec{W}_{l'}$. The coefficients B_l that minimize the power requirement are then the components of the eigenvector of S^{ij} with the largest-modulus eigenvalue. We call this protocol F -matrix AMFM (see Supplemental Material Sec. S1 for expanded mathematical details).

In Fig. 1(b) we show the infidelity computed according to F -matrix AMFM as a function of $L_{\text{cut}} = N_A - L_{\text{cut}}$, the complement of L_{cut} with respect to N_A . We observe that the infidelity rapidly decreases with increasing L_{cut} , reaching 10^{-4} at $L_{\text{cut}} \geq 9$. This infidelity is deemed acceptable in contemporary experiments, given that it roughly corresponds to the spontaneous scattering limit [31, 32]. This shows that a large number of eigenvectors of F may indeed be used as the variational space for minimizing the power with only a negligible fidelity cost.

In Fig. 1(c) we compare the power requirement of F -matrix AMFM with that of the exact AMFM as a function of gate duration τ . We see that F -matrix AMFM provides a power advantage for $\tau \lesssim 50 \mu\text{s}$ for qubit pair (1, 11) in a 15-ion, 11-qubit chain.

An important feature of the exact AMFM is its ability to actively introduce robustness against experimental parameter drift and fluctuations. While, in principle, the F -matrix approach can be stabilized as well, the following approach is more straightforward to implement.

We can relax the stringent requirement of perfect decoupling between the qubit and motional states as an alternative way to introduce a negligible amount of infidelity. According to the exact AMFM protocol this may be accomplished by constructing an approximate null space of M that now also includes eigenvectors with non-zero eigenvalues, as long as their moduli are smaller than a pre-determined, non-zero value. The Supplemental Material Sec. S2 contains expanded mathematical detail. Figure 1(c) shows that the power requirement of this extended null-space (ENS) approach is nearly identical to the power requirement of the F -matrix approach. In Fig. 1(d) we compare the pulse-power requirements of stabilized pulses produced according to the exact AMFM method and the ENS method, for which implementation of the stability conditions is straightforward. Over a large span of gate times, the ENS method offers significant power savings for stabilized pulses. In particular, we find that for stability degree $K = 6$ and gate duration $\tau = 250 \mu\text{s}$, the power saving can be as large as a factor of 15.

We note that faster gates come with exponentially decreasing infidelity and increased natural stability against mode-frequency drift, even in the absence of active stabilization. We illustrate this in Fig. 2(a), which shows that increasing the gate speed from $40 \mu\text{s}$ to $10 \mu\text{s}$ reduces the infidelity by about 6 orders of magnitude, reaching below $f = 10^{-8}$ over a drift-frequency range larger than $\pm 10 \text{ kHz}$ at $\tau = 10 \mu\text{s}$. While pulses this short may not be practical, the stability they provide can be propagated to longer gates at the cost of power optimality by reducing the power and repeating the pulse sequence multiple

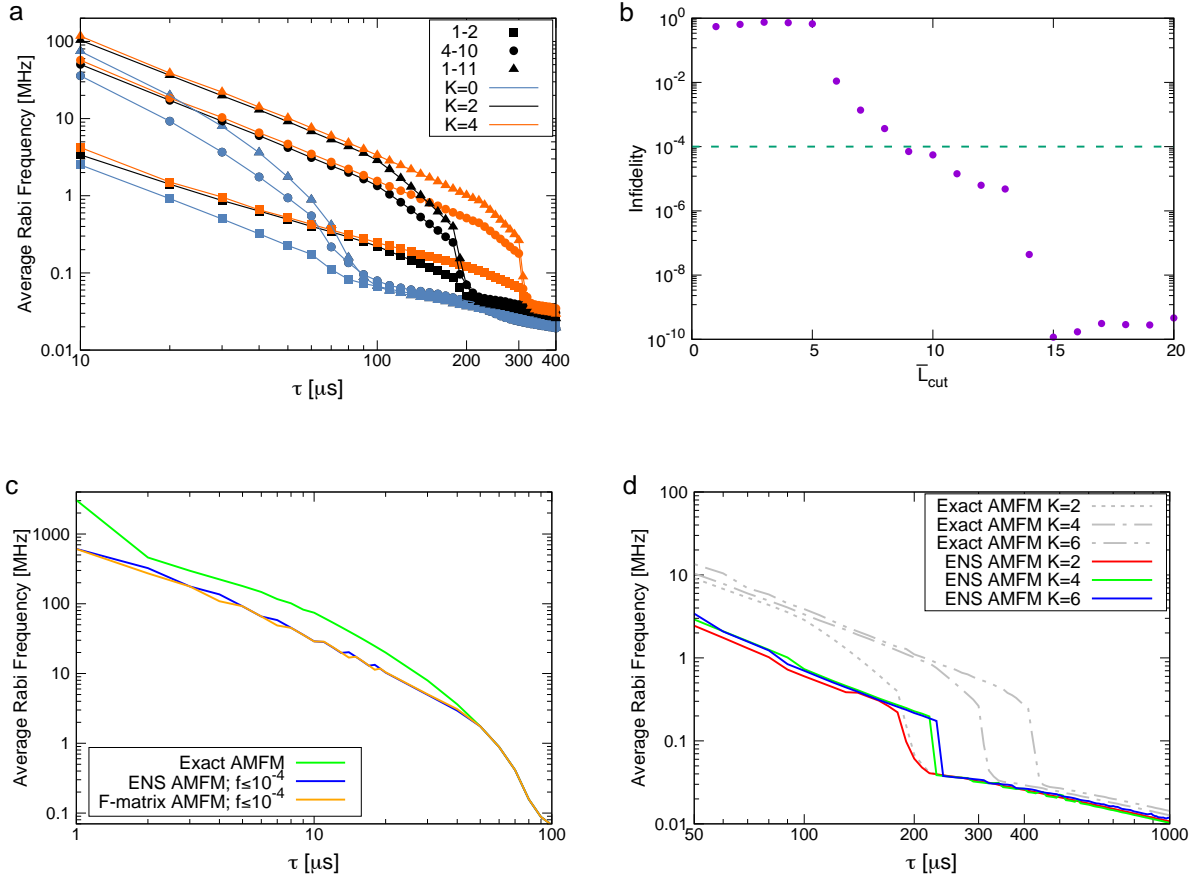


FIG. 1. Properties of gate pulses generated for a 15-ion, 11-qubit chain. (a) Power requirement of the exact AMFM gate as a function of gate time τ for three different qubit pairs, (1, 2) (squares), (4, 10) (circles), and (1, 11) (triangles), and three different degrees of stability $K = 0$ (blue), $K = 2$ (black), and $K = 4$ (orange). (b) Infidelity f as a function of \bar{L}_{cut} for $\tau = 150 \mu\text{s}$ gate pulses on qubits (1,11). A horizontal line at $f = 10^{-4}$, an acceptable amount of f for contemporary experiments, was placed to guide the eye. (c) Three-way comparison of average power requirement between exact AMFM (green), F matrix AMFM (orange), and ENS AMFM (blue), as a function of gate duration τ satisfying $f \leq 10^{-4}$. (d) Average power requirement as a function of τ for different degrees of stabilization K for the ENS protocol (colored, solid lines) with $f \leq 10^{-4}$. Red, green, and blue lines are for $K = 2$, $K = 4$, and $K = 6$, respectively. For comparison, the results for the exact AMFM for $K = 2$ (dotted line) and $K = 4$ (dot-dashed line) are copied from (a) without change, and $K = 6$ (dot-dot-dashed line) is added to illustrate the trend.

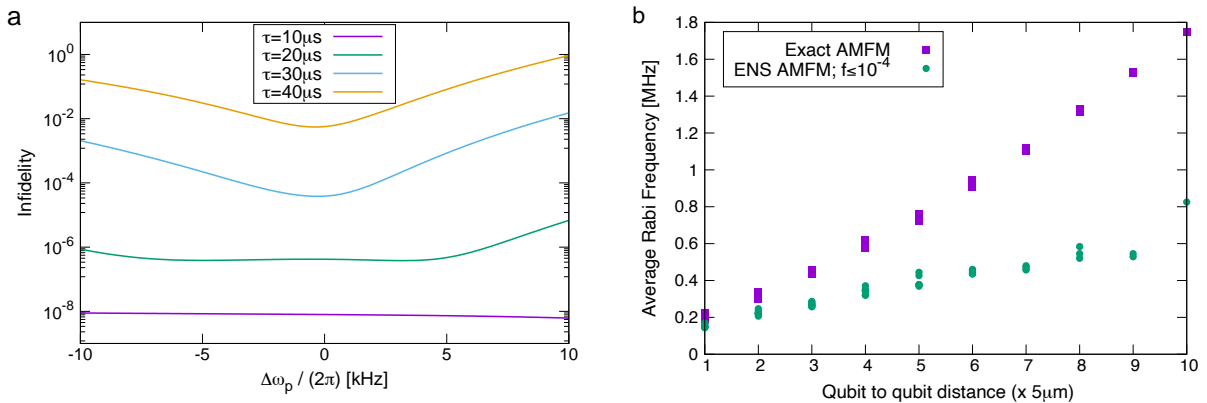


FIG. 2. Trade space for a 15-ion, 11-qubit chain. (a) Infidelity f as a function of uniform mode-frequency drift $\omega_p \rightarrow \omega_p + \Delta\omega_p$ on qubits (1, 11) ($\bar{L}_{\text{cut}} = 12$) for four different gate times τ . (b) Average power requirement as a function of distance between the qubits for a $\tau = 50 \mu\text{s}$ gate. Purple squares: exact AMFM; green circles: F -matrix protocol.

times.

According to Fig. 1(a) qubit pairs that are farther

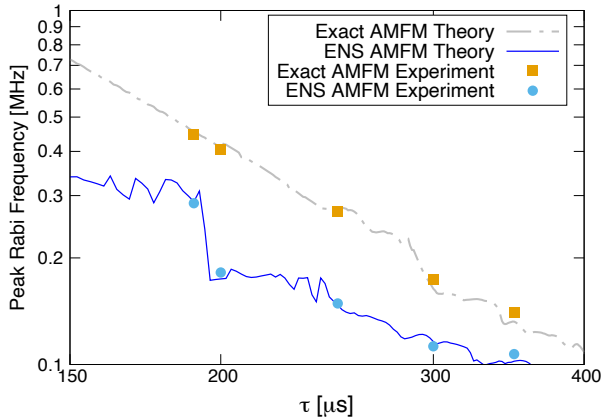


FIG. 3. Comparison of peak power requirements of ENS gates (blue solid line) with exact AMFM gates (grey dashed line) on qubits (4, 5) as a function of gate time τ ($K = 4$) for $f \leq 10^{-4}$ on a seven-ion, five-qubit chain. Experimental results for different gate times, implementing pulses constructed according to the exact AMFM and ENS protocols, are shown as orange squares and blue circles, respectively. The experimental error bars are smaller than the plot symbols.

apart from each other require more power. Therefore, given a fixed power budget, instead of trading the power savings afforded by our pulse design for gate duration, we can alternatively trade the savings for better qubit connectivity. This power-connectivity trade-off can play a critical role in harnessing the power of quantum computation since matching hardware and application connectivity is crucial for performance in a future quantum operating system [33]. In Fig. 2(b) we show the power requirement for $\bar{L}_{\text{cut}} = 12$ and $\tau = 50 \mu\text{s}$ as a function of qubit distance for the exact AMFM and the F -matrix AMFM. We see that the F -matrix AMFM requires factors of about 2 to 4 smaller power when compared to the exact AMFM counterparts.

Experiment.— We implement the exact AMFM and ENS pulses on a programmable, fully-connected trapped-ion quantum computer at the University of Maryland [34]. We trap seven $^{171}\text{Yb}^+$ ions in a 1D chain and use the middle five as qubits. The ions are laser-cooled close to the motional ground state, and then optically pumped to $|0\rangle$. Coherent operations are driven by a pair of counter-propagating Raman beams, one of which is split into individual addressing beams, each focused on one ion. These beams are controlled independently by RF pulses generated by arbitrary waveform generators (AWGs), which enable the implementation of pulse shapes from a broad range of frequencies, amplitudes, and phases.

Figure 3 shows the theoretically predicted and experimentally measured power requirements as a function of

gate duration for exact AMFM and ENS-based pulses. We chose infidelity $f = 10^{-4}$ to determine the ENS since the gates are limited to 10^{-2} by other imperfections. We chose to stabilize these pulses to degree $K = 4$.

Due to the limited amplitude resolution of the AWG (14-bit DAC), the relative amplitudes of basis frequencies smaller than 10^{-4} are neglected in the experimental implementation. We confirm numerically that this does not significantly impact the theoretical fidelity and stability of the resulting gates. We verify a successful implementation of a pulse by observing a continuous coherent transfer of population between the $|00\rangle$ and $|11\rangle$ states when the applied laser power is varied. We then calculate the minimal Rabi frequency $\Omega_0 = s\Omega_{\text{max}}$ needed to perform a maximally entangling gate, where $s \leq 1$ is a scale factor and Ω_{max} is the maximum Rabi rate available. We further verify the creation of the maximally entangled state by measuring the parity contrast for some of the pulses [7].

All the experimentally determined Rabi frequencies for the two-qubit gates using either the ENS- or the exact AMFM protocols fall within $\pm 10\%$ of the respective theoretically predicted values. The small discrepancies between experimental values and theory predictions are due to uncertainties in the Lamb-Dicke parameters and mode frequencies (see Supplemental Materials S4).

Finally, we verify the robustness of the gate solutions against drifts in the motional modes. We compare the phase space loop closure of an ENS gate stabilized to two different degrees, $K = 1$ and $K = 5$. The results, described in the Supplemental Material S3, are consistent with predictions.

Outlook.— The impossible trinity formed by power, gate duration, and fidelity discussed and illustrated in this paper has an analog in the chip design community, where there are well-known fundamental trade-offs between power, performance, and area, commonly referred to as PPA (see, e.g., [35]). Given that the physical-level infidelity affects, for instance, the cost of implementing quantum error correction to achieve a target logical-level infidelity, our investigations could be considered a quantum version of PPA trade-offs. Given the enormous utility and impact of a careful PPA study for system-on-a-chip design, our results may contribute to future quantum processor optimization. We are convinced that this holistic optimization of all facets of the design based on the PPA trade-off is another stepping stone toward successful practical quantum computing.

Acknowledgements.— We thank Cinthia Huerta Alderete and Yingyue Zhu for help with the experiment. N.M.L. acknowledges financial support from the NSF grant no. PHY-1430094 to the PFC@JQI, and the Maryland-ARL Quantum Partnership, grant no. W911NF1920181. A.M.G. is supported by a JQI Postdoctoral Fellowship.

-
- [1] F. Arute et al., Quantum Supremacy Using a Programmable Superconducting Processor, *Nature* **574**, 505 (2019).
- [2] <https://www.ibm.com/quantum-computing/> (Accessed September 13, 2020).
- [3] <https://www.rigetti.com> (Accessed September 13, 2020).
- [4] <https://www.honeywell.com/en-us/company/quantum> (Accessed September 13, 2020).
- [5] K. Wright et al., Benchmarking an 11-qubit Quantum Computer, *Nature Communications* **10**, 5464 (2019).
- [6] P. Schindler, D. Nigg, T. Monz, J. T. Barreiro, E. Martinez, S. X. Wang, S. Quint, M. F. Brandl, V. Nebendahl, C. F. Roos, M. Chwalla, M. Hennrich, and R. Blatt, A quantum information processor with trapped ions, *New J. Phys.* **15**, 123012 (2013).
- [7] T. Choi, S. Debnath, T. A. Manning, C. Figgatt, Z.-X. Gong, L.-M. Duan, and C. Monroe, Optimal Quantum Control of Multimode Couplings between Trapped Ion Qubits for Scalable Entanglement, *Phys. Rev. Lett.* **112**, 190502 (2014).
- [8] V. Kaushal et al., Shuttling-based trapped-ion quantum information processing, *AVS Quantum Sci.* **2**, 014101 (2020).
- [9] S. S. Elder et al., High-Fidelity Measurement of Qubits Encoded in Multilevel Superconducting Circuits, *Phys. Rev. X* **10**, 011001 (2020).
- [10] J. I. Colless et al., Computation of Molecular Spectra on a Quantum Processor with an Error-Resilient Algorithm, *Phys. Rev. X* **8**, 011021 (2018).
- [11] <https://github.com/Qiskit/ibmq-device-information> (Accessed September 12, 2020).
- [12] <https://pyquil-docs.rigetti.com/en/stable/compiler.html#compiler> (Accessed September 12, 2020).
- [13] D. Maslov, Basic circuit compilation techniques for an ion-trap quantum machine, *New J. Phys.* **19**, 023035 (2017).
- [14] C. D. Bruzewicz, J. Chiaverini, R. McConnell, and J. M. Sage, Trapped-Ion Quantum Computing: Progress and Challenges, *Appl. Phys. Rev.* **6**, 021314 (2019).
- [15] <https://aws.amazon.com/braket/hardware-providers/rigetti/> (Accessed September 12, 2020).
- [16] D. Leibfried, B. DeMarco, V. Meyer, D. Lucas, M. Barrett, J. Britton, W. M. Itano, B. Jelenković, C. Langer, T. Rosenband, and D. J. Wineland. Experimental demonstration of a robust, high-fidelity geometric two ion-qubit phase gate. *422(6930):412–415*, March 2003.
- [17] K. Mølmer, A. Sørensen, Multiparticle Entanglement of Hot Trapped Ions, *Phys. Rev. Lett.* **82**, 1835 (1999).
- [18] Anders Sørensen and Klaus Mølmer. Entanglement and quantum computation with ions in thermal motion. *Phys. Rev. A*, 62:022311, Jul 2000.
- [19] G.J. Milburn, S. Schneider, and D.F.V. James. Ion trap quantum computing with warm ions. *Fortschritte der Physik*, 48(9-11):801–810, 2000.
- [20] Shi-Liang Zhu, C. Monroe, and L.-M. Duan. Trapped ion quantum computation with transverse phonon modes. *Phys. Rev. Lett.*, 97:050505, Aug 2006.
- [21] S.-L. Zhu, C. Monroe, L.-M. Duan, Arbitrary-speed quantum gates within large ion crystals through minimum control of laser beams, *Europhys. Lett.* **73**, 485 (2006).
- [22] C. F. Roos, Ion trap quantum gates with amplitude-modulated laser beams, *New J. Phys.* **10**, 013002 (2008).
- [23] T. J. Green, M. J. Biercuk, Phase-modulated decoupling and error suppression in qubit-oscillator systems, *Phys. Rev. Lett.* **114**, 120502 (2015).
- [24] P. H. Leung, K. A. Landsman, C. Figgatt, N. M. Linke, C. Monroe, K. R. Brown, Robust 2-qubit gates in a linear ion crystal using a frequency-modulated driving force, *Phys. Rev. Lett.* **120**, 020501 (2018).
- [25] R. Blümel, N. Grzesiak, and Y. Nam, Power-optimal, stabilized entangling gate between trapped-ion qubits, <https://arxiv.org/abs/1905.09292> (2019).
- [26] Y. Shapira, R. Shaniv, T. Manovitz, N. Akerman, and R. Ozeri, Robust entanglement gates for trapped-ion qubits, *Phys. Rev. Lett.* **121**, 180502 (2018).
- [27] V. M. Schäfer et al., Fast quantum logic gates with trapped-ion qubits, *Nature* **555**, 75 (2018).
- [28] N. Grzesiak et al., Efficient arbitrary simultaneously entangling gates on a trapped-ion quantum computer, *Nature Communications* **11**, 2963 (2020).
- [29] C. Figgatt, A. Ostrander, N. M. Linke, K. A. Landsman, D. Zhu, D. Maslov, and C. Monroe. Parallel entangling operations on a universal ion-trap quantum computer. *Nature*, 572(7769):368–372, Aug 2019.
- [30] Yao Lu, Shuaining Zhang, Kuan Zhang, Wentao Chen, Yangchao Shen, Jialiang Zhang, Jing-Ning Zhang, and Kihwan Kim. Global entangling gates on arbitrary ion qubits. *Nature*, 572(7769):363–367, Aug 2019.
- [31] Y. Wu, S.-T. Wang, and L.-M. Duan, Noise analysis for high-fidelity quantum entangling gates in an anharmonic linear Paul trap, *Phys. Rev. A* **97**, 062325 (2018).
- [32] N. C. Brown and K. R. Brown, Comparing Zeeman qubits to hyperfine qubits in the context of the surface code: 174Yb^+ and 171Yb^+ , *Phys. Rev. A* **97**, 052301 (2018).
- [33] N. M. Linke, D. Maslov, M. Roetteler, S. Debnath, C. Figgatt, K. A. Landsman, K. Wright, C. Monroe, Experimental comparison of two quantum computing architectures, *Proc. Natl. Acad. Sci. U.S.A.* **114**, 3305 (2017).
- [34] K. A. Landsman, C. Figgatt, T. Schuster, N. M. Linke, B. Yoshida, N. Y. Yao, and C. Monroe. Verified quantum information scrambling. *Nature*, 567(7746):61–65, Mar 2019.
- [35] A. Teman, D. Rossi, P. A. Meinerzhagen, L. Benini, and A. P. Burg, Power, Area, and Performance Optimization of Standard Cell Memory Arrays Through Controlled Placement, *ACM Transactions on Design Automation of Electronic Systems* **21**, 59 (2016).
- [36] D. J. Wineland, C. Monroe, W. M. Itano, D. Leibfried, B. E. King, D. M. Meekhof, *Experimental Issues in Coherent Quantum-State Manipulation of Trapped Atomic Ions*, J. Res. Natl. Inst. Stand. Technol. **103**, 259–328 (1998).
- [37] S.Olmschenk, K.C. Younge, D.L. Moehring, D.N. Matsukevich, P.Maunz, and C.Monroe. Manipulation and detection of a trapped Yb + hyperfine qubit. *Phys. Rev. A*, **76**, 052314 (2007).

SUPPLEMENTAL MATERIAL

S1. F-MATRIX PROTOCOL

To start, we expand the laser pulse shape $g(t)$ as a Fourier-sine series

$$g(t) = \sum_{n=1}^{N_A} A_n \sin\left(\frac{2\pi n}{\tau} t\right), \quad (\text{S1})$$

where A_n , $n = 1, \dots, N_A$, are real expansion amplitudes, N_A is chosen large enough to achieve convergence, and τ is the gate time. We require the pulse shape to satisfy the stabilized phase-space closure conditions $\alpha_p^i(\tau)$, i.e.,

$$\left(\frac{\partial^k}{\partial \omega_p^k}\right) \alpha_p^i(\tau) = -\left(\frac{\partial^k}{\partial \omega_p^k}\right) \eta_p^i \int_0^\tau g(t) e^{i\omega_p t} dt = 0 \quad (\text{S2})$$

for $k = 0, 1, \dots, K$, where K is the desired degree of stabilization with respect to the motional-mode frequencies ω_p , $p = 1, \dots, N$, $i = 1, \dots, N$ is the ion-number index, N is the number of ions, $g(t)$ is the pulse function defined in (S1), and η_p^i is the Lamb-Dicke parameter [36], which describes the coupling strength of ion number i to motional-mode number p .

The two-qubit gate infidelity due to inexact phase space closure at zero temperature is given by [31]

$$f = \left(\frac{4}{5}\right) \sum_{p=1}^N (|\alpha_p^i(\tau)|^2 + |\alpha_p^j(\tau)|^2), \quad (\text{S3})$$

where i, j are qubit indices, p is the motional-mode index, and $\alpha_p^i(\tau)$ is defined in (S2). Inserting (S1) in (S2) with $k = 0$, we obtain

$$\begin{aligned} \alpha_p^i(\tau) &= -\eta_p^i \sum_{n=1}^{N_A} A_n \int_0^\tau \sin\left(\frac{2\pi n}{\tau} t\right) e^{i\omega_p t} dt \\ &= -\eta_p^i \sum_{n=1}^{N_A} A_n C_{np}, \end{aligned} \quad (\text{S4})$$

where

$$C_{np} = \int_0^\tau \sin\left(\frac{2\pi n}{\tau} t\right) e^{i\omega_p t} dt. \quad (\text{S5})$$

With this, f now becomes

$$f = \left(\frac{4}{5}\right) \sum_{p=1}^N \left\{ \left[(\eta_p^i)^2 + (\eta_p^j)^2 \right] \left(\sum_{n=1}^{N_A} A_n C_{np} \right)^2 \right\}, \quad (\text{S6})$$

which can be rewritten as

$$f = \left(\frac{4}{5}\right) \sum_{n=1}^{N_A} \sum_{m=1}^{N_A} A_n F_{nm} A_m, \quad (\text{S7})$$

where

$$F_{nm} = \sum_{p=1}^N \left[(\eta_p^i)^2 + (\eta_p^j)^2 \right] C_{np} C_{mp}, \quad (\text{S8})$$

and $m, n = 1, 2, \dots, N_A$. In matrix notation, we can express the matrix F according to

$$F = CDC^T, \quad (\text{S9})$$

where

$$D_{pp'} = \left[(\eta_p^i)^2 + (\eta_p^j)^2 \right] \delta_{pp'} \quad (\text{S10})$$

is a positive, diagonal matrix. This shows that F is positive semidefinite, i.e., it has only positive or zero eigenvalues. This is natural since f is semidefinite as well. The eigenvalues $\varphi_1 \leq \varphi_2 \leq \dots \leq \varphi_{N_A}$ of F determine the range of possible f values. We denote the normalized eigenvector of F corresponding to the eigenvalue φ_l by $\hat{V}^{(l)}$. Since F is real and symmetric, we have

$$\left[\hat{V}^{(l)} \right]^T \cdot \hat{V}^{(l')} = \delta_{l,l'}, \quad (\text{S11})$$

if $\varphi_l \neq \varphi_{l'}$, and in case of degeneracy, orthonormality can be achieved by orthogonalizing within the degenerate subspace. In order to obtain a relationship between infidelity and power, we compute the power in the space spanned by the eigenvectors of F , ranging from $\hat{V}^{(1)}$ to $\hat{V}^{(L_{\text{cut}})}$, where $L_{\text{cut}} \leq N_A$. Thus, for each choice of L_{cut} , we obtain an (infidelity, power) pair. Infidelity and power in the reduced space are computed in the following way. Expanding the vector \vec{A} into the chosen subspace of the eigenvectors $\hat{V}^{(1)}, \dots, \hat{V}^{(L_{\text{cut}})}$,

$$\vec{A} = \Omega_0 \sum_{l=1}^{L_{\text{cut}}} \hat{B}_l \hat{V}^{(l)}, \quad (\text{S12})$$

where Ω_0 is the pulse amplitude and

$$\sum_{l=1}^{L_{\text{cut}}} \hat{B}_l^2 = 1, \quad (\text{S13})$$

we obtain for the infidelity in the reduced space:

$$\begin{aligned} f &= \left(\frac{4}{5}\right) \vec{A}^T F \vec{A} \\ &= \left(\frac{4\Omega_0^2}{5}\right) \left[\sum_{l=1}^{L_{\text{cut}}} \hat{B}_l \hat{V}^{(l)T} \right] F \left[\sum_{l'=1}^{L_{\text{cut}}} \hat{B}_{l'} \hat{V}^{(l')} \right] \\ &= \left(\frac{4\Omega_0^2}{5}\right) \sum_{l=1}^{L_{\text{cut}}} \hat{B}_l^2 \varphi_l. \end{aligned} \quad (\text{S14})$$

It remains to compute \hat{B} . We start from the expression

for the entangling angle $\chi(\tau)$

$$\begin{aligned}\chi(\tau) &= \vec{A}^T \mathcal{K} \vec{A} \\ &= \Omega_0^2 \left[\sum_{l=1}^{L_{\text{cut}}} \hat{B}_l \hat{V}^{(l)T} \right] \mathcal{K} \left[\sum_{l'=1}^{L_{\text{cut}}} \hat{B}_{l'} \hat{V}^{(l')} \right] \\ &= \Omega_0^2 \sum_{l,l'=1}^{L_{\text{cut}}} \hat{B}_l S_{l,l'} \hat{B}_{l'},\end{aligned}\quad (\text{S15})$$

where

$$S_{l,l'} = \hat{V}^{(l)T} \mathcal{K} \hat{V}^{(l')}, \quad (\text{S16})$$

and

$$\begin{aligned}\mathcal{K}_{nm} &= \sum_{p=1}^N \eta_p^i \eta_p^j \int_0^\tau dt_2 \int_0^{t_2} dt_1 \sin\left(\frac{2\pi m}{\tau} t_1\right) \\ &\quad \sin\left(\frac{2\pi n}{\tau} t_2\right) \sin\left[\omega_p(t_2 - t_1)\right].\end{aligned}\quad (\text{S17})$$

Diagonalizing the reduced kernel matrix $S_{l,l'}$ in the subspace $1 \leq l, l' \leq L_{\text{cut}}$, we obtain its eigenvalues $\lambda_1, \lambda_2, \dots, \lambda_{L_{\text{cut}}}$. Finally, we find $\vec{B} = \vec{v}$, where \vec{v} is the normalized eigenvector of S corresponding to the eigenvalue λ_{max} with the largest absolute value. Thus, with (S15), we accomplish the maximally entangling gate, $\chi(\tau) = \frac{\pi}{8}$, with the minimal Ω_0 according to

$$\Omega_0 = \left(\frac{\pi}{8|\lambda_{\text{max}}|} \right)^{1/2}. \quad (\text{S18})$$

With (S13), we find that the infidelity (S14) satisfies

$$\frac{4\Omega_0^2 \varphi_1}{5} \leq f \leq \frac{4\Omega_0^2 \varphi_{L_{\text{cut}}}}{5}. \quad (\text{S19})$$

Therefore,

$$f_{\text{max}} = \left(\frac{4\Omega_0^2}{5} \right) \varphi_{L_{\text{cut}}} \quad (\text{S20})$$

is a rigorous upper bound of the infidelity f .

S2. EXTENDED NULL-SPACE PROTOCOL

The extended null-space method presented here is an alternative way to generate efficient AMFM control pulses that satisfy $\alpha_p^i(\tau) \approx 0$ for all i and p . Conceptually, the pulse construction relies on a procedure similar to that in (S11)-(S13), and offers similar savings in the peak power levels of resulting pulses. Specifically, whereas L_{cut} controls the number of eigenvectors of matrix F included in the chosen solution subspace [see Supplementary Material Section S1, equation (S12)], here, the subspace is formed only by eigenvectors of the matrix Γ , defined in (S23), whose eigenvalues, in absolute magnitude, are smaller than some threshold Z . Thus, by

adjusting the value of Z , we allow for additional eigenvectors of Γ , other than null-space vectors with eigenvalue zero, to be included in the solution subspace.

In the exact AMFM approach, described in detail in Ref. [25], the aim is to find the null space of the matrix M , i.e., the set of $N_0 = N_A - N(K+1)$ linearly independent, nontrivial vectors $\vec{A}^{(\alpha)}$, $\alpha = 1, \dots, N_0$, that satisfy

$$\begin{aligned}& - \left(\frac{\partial^k}{\partial \omega_p^k} \right) \eta_p^i \sum_{n=1}^{N_A} A_n \int_0^\tau \sin\left(\frac{2\pi n}{\tau} t\right) e^{i\omega_p t} dt \\ &= \sum_{n=1}^{N_A} M_{mn} A_n = M \vec{A} = 0,\end{aligned}\quad (\text{S21})$$

where the matrix M contains the stabilized phase-space closure conditions defined under Eq. (S2). In order for (S21) to have non-trivial solutions, we require that $N_A > N(K+1)$. Thus, in general, the rank-deficient, rectangular matrix M has $N(K+1)$ non-zero eigenvalues and $N_0 = N_A - N(K+1)$ zero eigenvalues. This suggests to multiply (S21) from the left with the transpose, M^T , of M , which turns (S21) into

$$\Gamma \vec{A} = 0, \quad (\text{S22})$$

where

$$\Gamma = M^T M \quad (\text{S23})$$

is a symmetric matrix. Section S17 of Supplemental Material of Ref. [25] shows that the operation of multiplication with M^T does not change the structure of the solution space.

Where the exact AMFM approach allows only the N_0 null-space vectors of Γ with $\lambda_j = 0$, $j = 1, \dots, N_0$, and satisfies (S22) exactly, here, we include additional eigenvectors in an extended “null”-space of dimension larger than N_0 that correspond to non-zero eigenvalues of Γ . Diagonalizing Γ , we obtain its eigenvalues $\lambda_1, \lambda_2, \dots, \lambda_{N_A}$, ordered according to the size of their absolute values, such that

$$0 \leq |\lambda_1| \leq |\lambda_2| \leq \dots \leq |\lambda_{N_A}|. \quad (\text{S24})$$

Since the magnitude of each non-zero eigenvalue is proportional to the magnitude of violation of (S22), we define a parameter Z (e.g., $Z = 10^{-4}$) and include only eigenvalues whose absolute magnitude is smaller than Z in the extended “null”-space. With this definition of the extended “null”-space, the power optimization procedure follows (S15)-(S18) with N'_0 in place of L_{cut} , where N'_0 , the dimension of the extended “null”-space, is given by

$$N'_0 = N_A - N(K+1) + N_{\text{ENS}}, \quad (\text{S25})$$

where N_{ENS} is the number of eigenvectors of Γ whose eigenvalues are greater than 0 but less than Z in their absolute values, $N_{\text{ENS}} \in [0, N(K+1)]$, and ENS stands for

“Extended Null Space”. By allowing additional eigenvectors of Γ into the solution subspace, we effectively relax the last line of (S21) into

$$M\vec{A} \approx 0, \quad (\text{S26})$$

which yields control pulses with lower power than does the exact AMFM protocol.

S3. STABILIZED GATE DEMONSTRATION

We demonstrate the benefit of stabilizing the gates with respect to fluctuations in the motional mode frequencies presented in the paper, by applying pulses with two different stabilization orders $K = 1$ and $K = 5$ to qubits (4,5) on our seven-ion, five-qubit quantum computer. The two ENS AMFM pulses are designed for theoretical $f \leq 10^{-4}$ at zero gate frequency offset. To systematically control the detuning error, we offset the gate frequency from the original intended gate frequency, which is equivalent to uniformly offsetting the motional mode frequencies in the opposite direction. Figure S1 shows the even-parity population $P_{\text{even}} = P_{00} + P_{11}$, which is a proxy for the gate fidelity, as a function of gate frequency offset. We apply the pulses to the initial state $|00\rangle$ and measure the even-parity populations when $P_{00} \approx P_{11}$, akin to performing a maximally entangling gate. The experimentally measured values with their associated error bars are marked in green. The error bars are 1σ confidence intervals, sampled from a binomial distribution, and each point represents 4000 experimental shots. The blue line shows the analytical fidelity

$$\bar{F} = 1 - \frac{4}{5} \sum_p (|\alpha_{i,p}|^2 + |\alpha_{j,p}|^2), \quad (\text{S27})$$

which is valid in the low-infidelity limit [31]. The width of the detuning-robust region is greater for the pulse with the higher stabilization order $K = 5$ than for the pulse with $K = 1$.

S4. EXPERIMENTAL DETAILS

In this section, we describe in detail the experimental setup and procedures. We encode the $|0\rangle$ and $|1\rangle$ qubit states in the two hyperfine levels $|F = 0, m_F = 0\rangle$, $|F = 1, m_F = 0\rangle$ of the ground state $^2S_{1/2}$ of $^{171}\text{Yb}^+$. The qubit frequency is given by the hyperfine splitting $\omega_{HF} = 2\pi \times 12.6428$ GHz and is magnetic field insensitive to first order [37]. The ions are confined radially by an RF field at $\omega_{RF} = 2\pi \times 23.83$ MHz and axially by a static field. The radial standard pseudo-frequency in the transverse gate direction, denoted X is $\omega_7 = 2\pi \times 3.054(1)$ MHz. In all of our experiments, we employ a two-step cooling process on the X modes with Doppler cooling to $\bar{n} \approx 10$ and sideband cooling to

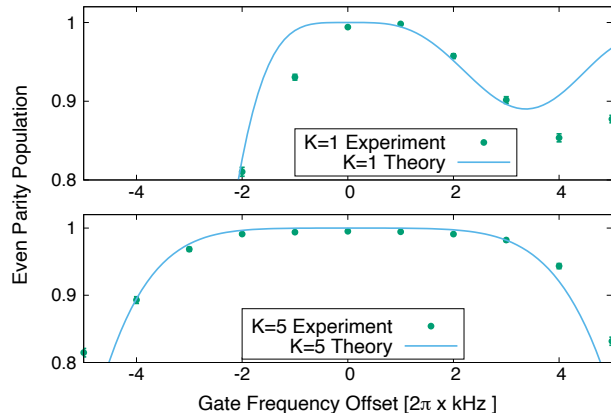


FIG. S1. Experimental demonstration of the K -order stabilized two-qubit gates for qubit pair (4,5) on our seven-ion, five-qubit quantum computer. The ENS AMFM pulse sequence satisfying $f \leq 10^{-4}$ at no frequency offset with $K = 1$ (top) and $K = 5$ (bottom), corresponds to a maximally entangling gate. The experimentally measured even-parity population is plotted as a function of the gate frequency. The blue lines show the gate fidelity according to the analytical expression in (S27), valid in the low-error limit. The width of the detuning-robust region is greater for the pulse with the higher stabilization order $K = 5$ than for the pulse with $K = 1$.

$\bar{n} \approx 0.1$. As described in the main text, the qubit transition can be driven coherently with a pair of counter-propagating Raman beams at 355 nm, controlled individually by a 32-channel AOM using RF pulses. We can adjust the beatnote of the Raman beams by changing the RF frequencies to address the qubit, the blue sideband or the red sideband transition. Finally, projective measurements are performed with state-dependent fluorescence on an array of photomultiplier tubes (PMT) with 98.4(1)% readout fidelity for a two-qubit state and 95(1)% readout fidelity for a five-qubit state.

To accurately determine the experimental Rabi frequencies for every two-qubit gate presented in Fig. 3, we employ the following procedure. To eliminate the effect of beam alignments and laser power fluctuation on the Rabi frequencies, for each experiment, we measure the carrier Rabi frequencies of each qubit at the scale $s = 1$. We then scan the scale to observe coherent population transfer between $|00\rangle$ and $|11\rangle$, a signature of the MS gate. From this scan, we can determine the scale for maximally entangling gate. We perform the gate at this scale with 10000 data points and correct for state-preparation and measurement (SPAM) errors in post-processing to obtain a good estimate of the scale, and therefore the Rabi rate Ω_0 .

A carefully designed protocol for accurately determining the motional mode frequencies as well as the Lamb-Dicke parameters η_p^2 is necessary to achieve a good agree-

ment between predicted and observed Rabi rates needed for a maximally entangling gate. Here, we present the details of the protocol we implement in terms of experimental procedures and post processing steps. Experimentally, we aim to measure the mode frequencies and the magnitude of the Lamb-Dicke parameters through sideband spectroscopy.

After ground-state cooling and initialization, we scan the frequencies across the blue sideband for each ion, one ion at a time, with square pulses at a fixed laser power and pulse duration before detecting the population in $|1\rangle$ state. For each normal mode and each ion, we can define a sideband Rabi frequency as $\Omega_i^p = \sqrt{\bar{n} + 1}\Omega_i\eta_i^p$, where Ω_i is the Rabi frequency of the qubit transition. When Ω_i^p is much smaller than the splitting between motional mode frequencies, the transitions with frequency in the vicinity of the motional mode frequency ω_p can be modeled as a two-level system and the final $|1\rangle$ state population after a pulse with a duration t_{bsb} can be approximated as

$$P_{|1\rangle} = \frac{\Omega_i^{p2}}{\Omega_i^{p2} + \delta\omega_p^2/4} \sin^2 \left(t_{\text{bsb}} \sqrt{\Omega_i^{p2} + \frac{\delta\omega_p^2}{4}} \right), \quad (\text{S28})$$

where $\delta\omega_p$ is the difference between the mode frequency ω_p and the frequency of the sideband pulse. Thus, with enough frequency points scanned near each mode, we can fit the qubit $|1\rangle$ state population as a function of frequency to (S28) and extract ω_p and $|\Omega_i^p|$. Note that we

choose the pulse duration and the Rabi frequency of the qubit transition with care so that $P_{|1\rangle} \lesssim 50\%$ to minimize the effect of the thermal distribution of the mode phonon population. Using the Rabi frequency of the qubit transition, which can be measured in a straightforward fashion, the magnitude of the Lamb-Dicke parameter is given by $|\eta_i^p| = |\Omega_i^p|/\sqrt{\bar{n} + 1}\Omega_i$. After measuring them for all modes and addressable ions, we fit the magnitudes and the mode frequencies to a simple theoretical model of a linear ion chain and obtain theoretically fitted η_i^p , including their signs. The model includes the Coulomb interaction between ions and individual harmonic confinements for each ion along the direction that is perpendicular to the chain. The inter-ion spacing and the spring constants for the harmonic confinements are the fit parameters. An example of the fitted Lamb-Dicke parameters is shown in Fig. S2, which shows the quality of the fit is excellent. For increasingly small η_i^p values, measuring them precisely and accurately becomes difficult, since the BSB Rabi frequencies Ω_i^p are smaller than the frequency resolution of the scan (which is 1.5 kHz), and the measurements become dominated by RF noises of the trap. Therefore, it is more appropriate to use the theoretically fitted Lamb-Dicke parameters for the pulse-shaping calculations.

The mode frequencies used to generate the pulses are reported in Table S1. Figures S3 and S4 show the pulse shapes used to implement the two-qubit gates on our seven-ion, five-qubit trapped-ion quantum computer.

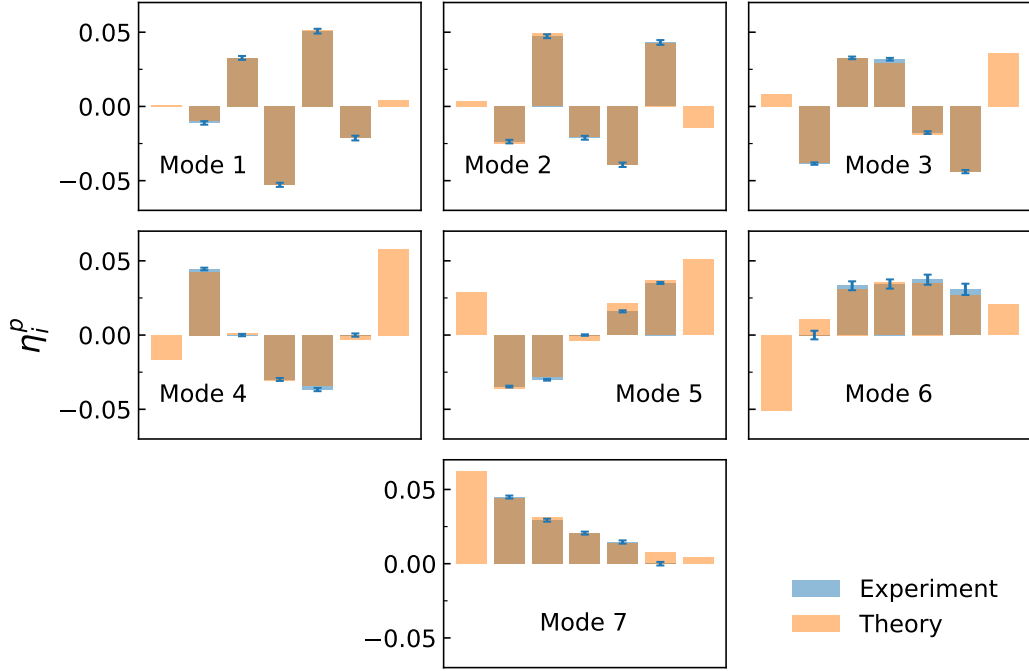


FIG. S2. Comparison between experimentally extracted Lamb-Dicke parameters and theoretically fitted ones. The signs of the experimentally extracted Lamb-Dicke parameters are forced to be the same as the theoretically predicted ones since we can only extract the magnitude of the Lamb-Dicke parameters using sideband spectroscopy. The blue bars are experimental measurements. The blue error bars are statistical errors propagated through the fitting routines by bootstrap. The error bars do not account for systematic errors such as mode drift, heating and motional decoherence during the measurements. Only the middle five ions are accessible by Raman lasers thus there is not any data for the two ions at the ends of the chain. The orange bars represent the fitted result using the simple theoretical model described in SM Sec. S4. The modes are indexed in the order of increasing mode frequency, as shown in Tb. S1.

Mode	$\omega_p/2\pi$ (MHz)
1	2.951
2	2.973
3	2.993
4	3.010
5	3.025
6	3.038
7	3.054

TABLE S1. Mode frequencies of the motional modes of our seven-ion chain.

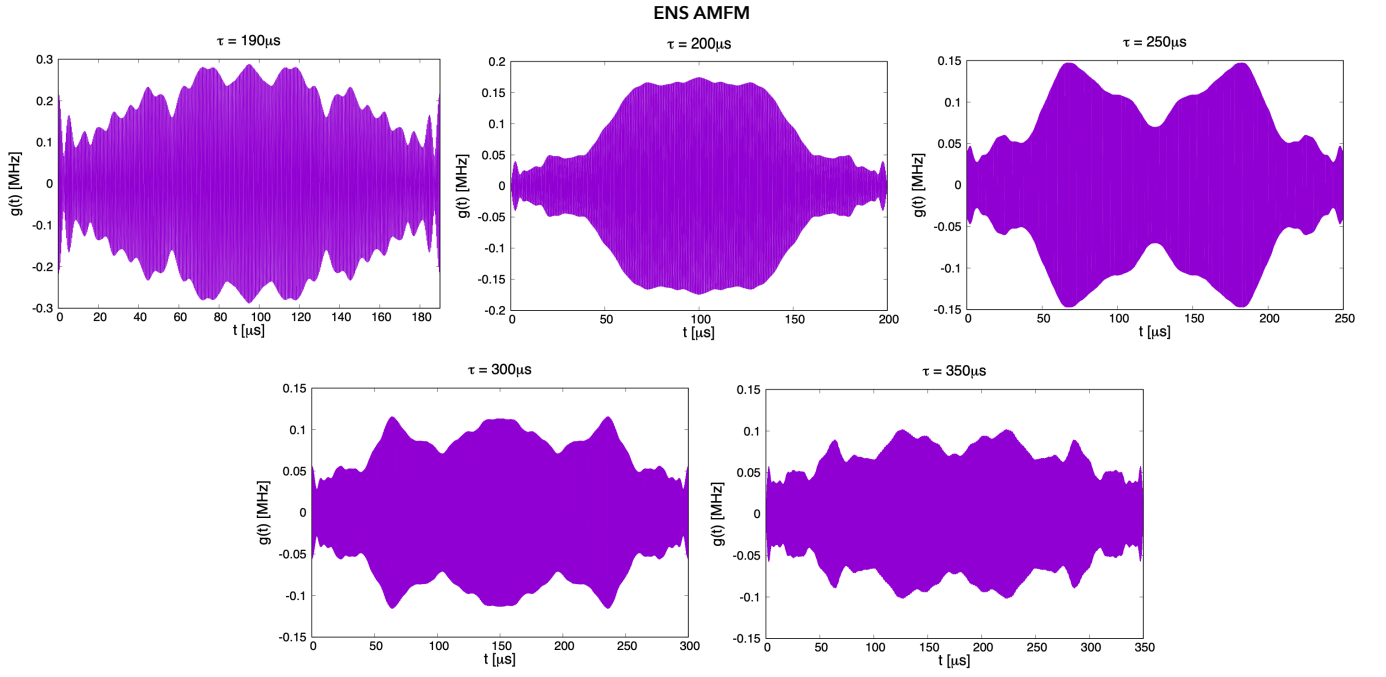


FIG. S3. Pulse shapes for two-qubit gates on qubits 4, 5 computed according to the extended null-space AMFM protocol.

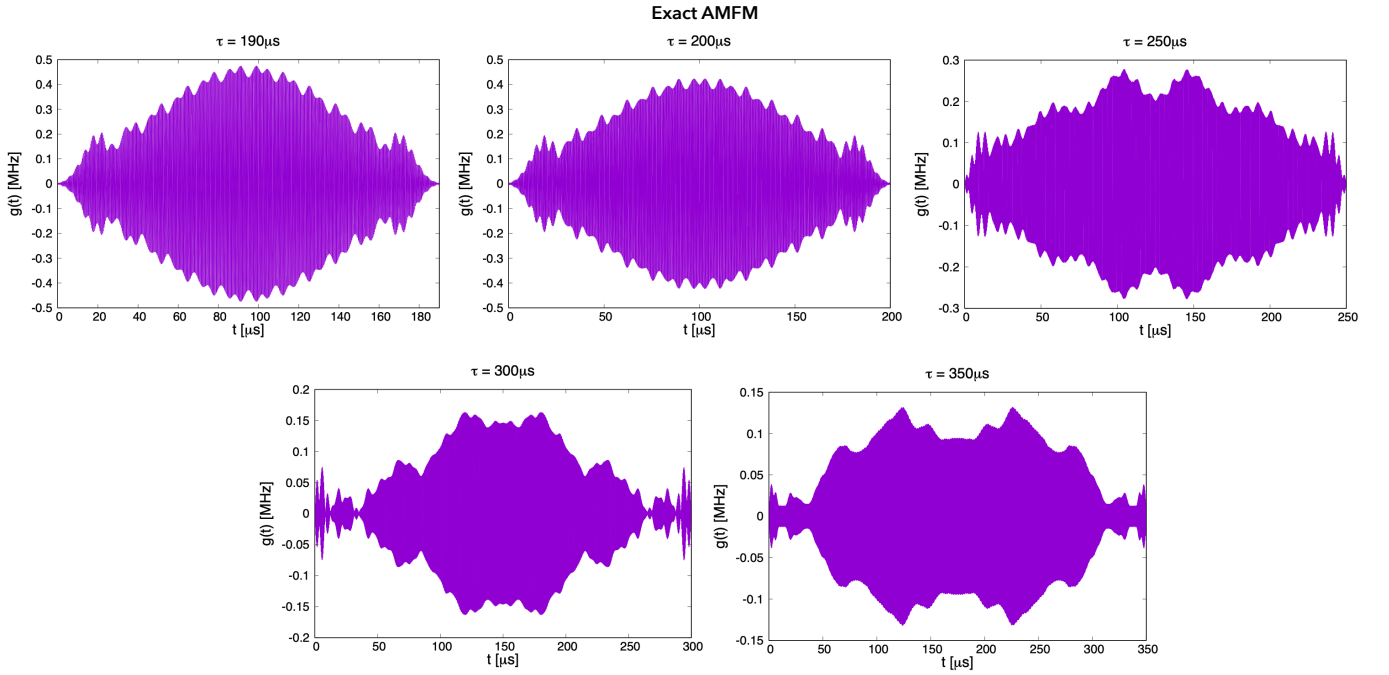


FIG. S4. Pulse shapes for two-qubit gates on qubits 4, 5 computed according to the exact AMFM protocol.